Small

NANO · MICRO small
www.small-journal.com

RESEARCH ARTICLE

Ultrafast 60-Second Synthesis of Meter-Scale Ni-based Catalysts via Phosphomolybdic Acid Complexation for Durable Seawater Oxidation at 1 A cm^{-2}

Xianhang Huang[1] | Luyu Chen[1] | Yingyao Li[1] | Yeqing Liu[1] | Hang Zhang[1] | Lejia Li[2] | Yu Wang[1,3,4]

[1]South China Advanced Institute for Soft Matter Science and Technology, School of Emergent Soft Matter, South China University of Technology, Guangzhou, China | [2]School of Microelectronics, South China University of Technology, Guangzhou, China | [3]Center for Electron Microscopy, South China University of Technology, Guangzhou, China | [4]Guangdong Provincial Key Laboratory of Functional and Intelligent Hybrid Materials and Devices, South China University of Technology, Guangzhou, China

Correspondence: Yu Wang (roywangyu@scut.edu.cn)

Received: 27 October 2025 | **Revised:** 17 December 2025

Keywords: industrial-scale fabrication | interfacial etching | oxygen evolution catalyst | seawater electrolysis

ABSTRACT

Direct seawater electrolysis offers a sustainable pathway for hydrogen production, yet the development of cost-effective catalysts with high activity, durability, and scalable preparation remains challenging. Here, we report a mild interfacial synergistic etching strategy that enables the rapid fabrication of efficient oxygen evolution catalysts. Nickel foam is controllably etched by phosphomolybdic acid (PMA) and trace Fe^{3+}, yielding meter-scale catalysts (60-Fe-PMA/NF) within 60 s at room temperature. The synergistic incorporation of iron and the dynamic leaching–reabsorption of phosphomolybdate in alkaline media promote rapid surface reconstruction, enhancing chloride corrosion resistance and impurity tolerance. As a result, 60-Fe-PMA/NF exhibits superior stability under harsh seawater electrolysis conditions. In a zero-gap electrolyzer, it operates steadily for more than 270 h at 1.0 A cm^{-2} in alkaline seawater (1 M KOH + seawater). This work demonstrates a scalable, low-cost strategy for constructing robust OER catalysts, advancing practical seawater electrolysis toward sustainable hydrogen production.

1 | Introduction

Hydrogen is widely recognized as a pivotal energy carrier for decarbonizing hard-to-abate sectors (industry, transportation, construction) and enabling global energy storage through renewable integration [1, 2]. The convergence of offshore wind power expansion and freshwater scarcity has intensified interest in direct seawater electrolysis for green hydrogen production [3]. Within water electrolysis, the anodic oxygen evolution reaction (OER) imposes severe kinetic limitations due to its complex four-electron transfer process. These challenges are exacerbated in seawater by competitive chloride oxidation at the anode, where high chloride (Cl^-) concentrations reduce OER selectivity, accelerate catalyst corrosion, and compromise durability. These issues become critical at industrial current densities (> 500 mA cm^{-2})—a regime essential for practical deployment. While recent seawater OER catalysts achieve moderate stability at ⩽ 500 mA cm^{-2} [4–7], operational durability exceeding 200 hours at > 500 mA cm^{-2} remains exceptionally rare.

Nickel-based electrodes (e.g., foam, mesh, Raney Ni) dominate commercial alkaline electrolyzers due to their cost-effectiveness and bifunctional activity [8, 9]. However, they suffer rapid degradation in alkaline seawater from chloride-induced corrosion [10, 11], limiting their direct applicability. Recent advances in engineered Ni-based catalysts, such as NiFe-LDH@Co_9S_8-Ni_3S_2/NF (298 mV @ 1000 mA cm^{-2}) [12] and NiFeV/NF (240 h @ 500 mA cm^{-2}) [13], demonstrate promising seawater OER performance.

Nevertheless, these often rely on energy-intensive syntheses (e.g., solvothermal, electrodeposition), which are prohibitively costly for meter-scale production. Alternatively, immersion-based methods enable room temperature fast synthesis with scalability [14, 15], but the short immersion time generally leads to insufficient chemical stability of the catalyst/support interface, causing inadequate chloride tolerance at industrial currents (> 500 mA cm^{-2}). Thus, a critical gap persists: scalable fabrication of chloride-resistant OER catalysts that sustain high activity and stability under industrial current densities.

Herein, we develop an ultrafast room temperature synthesis of high-performance Ni-based OER catalysts by introducing phosphomolybdic acid (PMA) into the immersion solution. PMA's inherent acidity, polyanionic framework, and strong metal-binding capacity collectively assure the chemical stability of the catalyst/support interface during the OER at industrial currents. This strategy enables meter-scale fabrication via 60-s immersion of Ni foam in PMA/$FeCl_3$ solution. The resulting catalyst exhibits outstanding OER activity in alkaline seawater (312 mV @ 100 mA cm^{-2}), significantly outperforming than Ni foam based controls (414–679 mV) and RuO_2 (524 mV). Integrated into a precious metal-free zero-gap electrolyzer (with NiMo foam cathode), the catalyst achieves 1.0 A cm^{-2} at 2.9 V in alkaline seawater (1 M KOH + seawater) with exceptional stability over 270 h. Mechanistic studies attribute the enhanced activity to accelerated hydroxide-to-oxyhydroxide transition kinetics at the catalyst-electrolyte interface, the exceptional durability to the PMA-promoted γ-NiOOH formation. This work establishes a scalable, cost-effective pathway to industrial seawater electrolysis.

2 | Results and Discussion

2.1 | Synthesis and Structural Characterization of PMA-Mediated OER Catalysts

The PMA-mediated OER catalysts were synthesized through the synergistic co-etching of nickel foam (NF) by PMA and Fe^{3+} via a one-step immersion process (Figure 1a). NF substrates were immersed for 60 seconds at room temperature in an aqueous solution containing 0.002 M PMA and 0.1 M $FeCl_3$, yielding the catalyst designated as 60-Fe-PMA/NF. In the precursor solution, positively charged Fe^{3+} ions coordinate with anionic phosphomolybdate species to form nanoscale ferric phosphomolybdate complexes [16, 17]. Simultaneously, Fe^{3+} and H^+ (from PMA's inherent acidity) etch the NF surface, accelerating Ni^{2+} dissolution, enhancing surface roughness, and enabling anchored deposition of ferric phosphomolybdate species. This ultrafast, room-temperature synthesis facilitates scalable production, as demonstrated by digital photographs of meter-scale catalysts (1.00 × 0.25 m; Figure 1b,d), where the NF transitions from metallic silver to brown while retaining structural integrity.

Scanning electron microscopy (SEM) confirms preservation of the 3D macroporous NF framework after 60-s etching, now uniformly coated with a surface sediment layer (Figure 1c,e). Control experiments highlight the critical synergy between Fe^{3+} and PMA: negligible surface modification occurred when NF was treated individually with $FeCl_3$ or PMA, or when PMA was substituted with silicomolybdic acid, phosphotungstic acid, or phosphoric acid-molybdate mixtures (Figure S1). High-resolution transmission electron microscopy (TEM) and high-angle annular dark-field scanning TEM (HAADF-STEM) further reveal that deposited particles on 60-Fe-PMA/NF exhibit irregular morphology and amorphous character, verified by selected-area electron diffraction (SAED; Figure 1f). This amorphous character is further corroborated by X-ray diffraction (XRD) and grazing-incidence XRD (GI-XRD) analyses. The conventional $\theta - 2\theta$ XRD pattern displays only diffraction peaks corresponding to the metallic Ni substrate, with no detectable reflections from crystalline catalyst phases (Figure S2). To enhance the sensitivity to the catalyst layer, GI-XRD measurements were performed on a model sample prepared on a thin Ni foil, revealing a broad diffuse halo in the 15–30° range (Figure S3), a hallmark of amorphous structures. Energy-dispersive X-ray spectroscopy (EDS) mapping further demonstrates homogeneous distribution of Ni, Fe, Mo, O, and P within these particles (Figures 1g and S4), confirming effective co-immobilization of PMA and Fe species on NF.

Raman spectroscopy (Figure S5) of 60-Fe-PMA/NF reveals the transition from the PMA-specific Mo–O–Mo and Mo–O peaks to the emergent Mo–O–Fe/Ni bonds, evidencing PMA anchoring to Ni/Fe sites [18]. Conversely, the Fe^{3+}-free control (60-PMA/NF) lacks discernible Mo–O–Fe/Ni Raman signatures, underscoring Fe^{3+}'s essential role in facilitating deposition. X-Ray photoelectron spectroscopy (XPS) analysis confirms the abundant presence of Fe, P, Mo, and O species on the catalyst surface (Figure S6). Inductively coupled plasma optical emission spectroscopy (ICP-OES) quantifies interfacial reactions (Table S1): Fe and Mo loadings in 60-Fe-PMA/NF (0.0520% Fe, 1.3937% Mo) significantly exceed those in mono-component controls (60-Fe/NF: 0.0269% Fe; 60-PMA/NF: 0.0099% Mo), conclusively demonstrating enhanced co-deposition efficiency through PMA-Fe^{3+} complexation.

2.2 | OER Performance in Alkaline Seawater

The OER performance of catalysts was evaluated in 1 M KOH and alkaline seawater (1 M KOH + seawater) via linear sweep voltammetry (LSV). As shown in Figure 2a, 60-Fe-PMA/NF demonstrated superior activity versus all controls (60-Fe/NF, 60-PMA/NF, RuO_2, and bare NF). Quantitative analysis at 100 mA cm^{-2} (Figure 2b) reveals that 60-Fe-PMA/NF achieves an overpotential of just 269 mV in 1 M KOH, outperforming 60-Fe/NF (274 mV), 60-PMA/NF (665 mV), bare NF (628 mV), and commercial RuO_2 (427 mV). Crucially, in alkaline seawater electrolyte, 60-Fe-PMA/NF maintains exceptional performance with only 312 mV overpotential, while comparative materials exhibit significant degradation: 60-Fe/NF (414 mV), 60-PMA/NF (676 mV), bare NF (679 mV), and RuO_2 (524 mV). The uniformity and reproducibility of the synthesis were confirmed by statistical analysis. Intra-batch uniformity was evaluated across nine locations on a single meter-scale electrode, giving a relative standard deviation (RSD) of 5.8% (Figure S7), while inter-batch reproducibility was tested across three independently prepared small-scale 15 cm^2 electrodes, yielding an RSD of 3.5% (Figure S8). These results indicate that the 60-s synthesis reliably produces consistent catalysts suitable for scalable production.As a practical benchmark, commercial Raney Ni requires 400 mV to reach

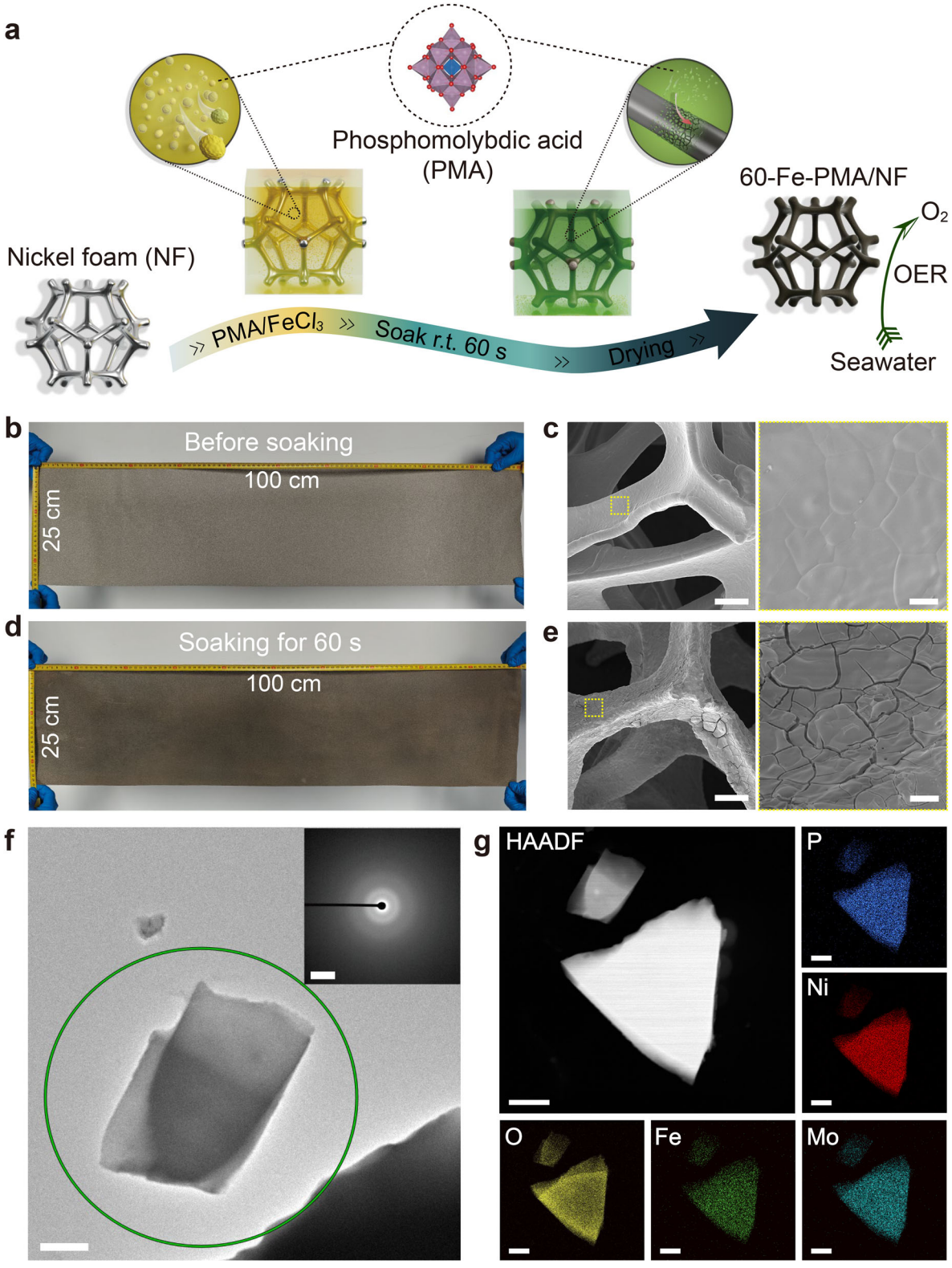

FIGURE 1 | Ultrafast synthesis and structural features of 60-Fe-PMA/NF. (a) Schematic of the room-temperature immersion synthesis: Nickel foam (NF) reacts with PMA/$FeCl_3$ solution within 60 s. (b) Photograph and (c) SEM images of pristine NF (metallic silver surface; smooth morphology). (d) Photograph and (e) SEM images of 60-Fe-PMA/NF (brown surface; uniform sediment layer coating intact 3D macroporous framework). (f) High-resolution TEM image and SAED pattern confirming amorphous structure of deposited particles. (g) HAADF-STEM image and EDS elemental maps showing homogeneous distribution of P, Ni, O, Fe, and Mo. Scalebar: (c) and (e), 50 μm (left), 5 μm (right); (f), 300 nm, 5 nm^{-1} (inset); (g), 500 nm.

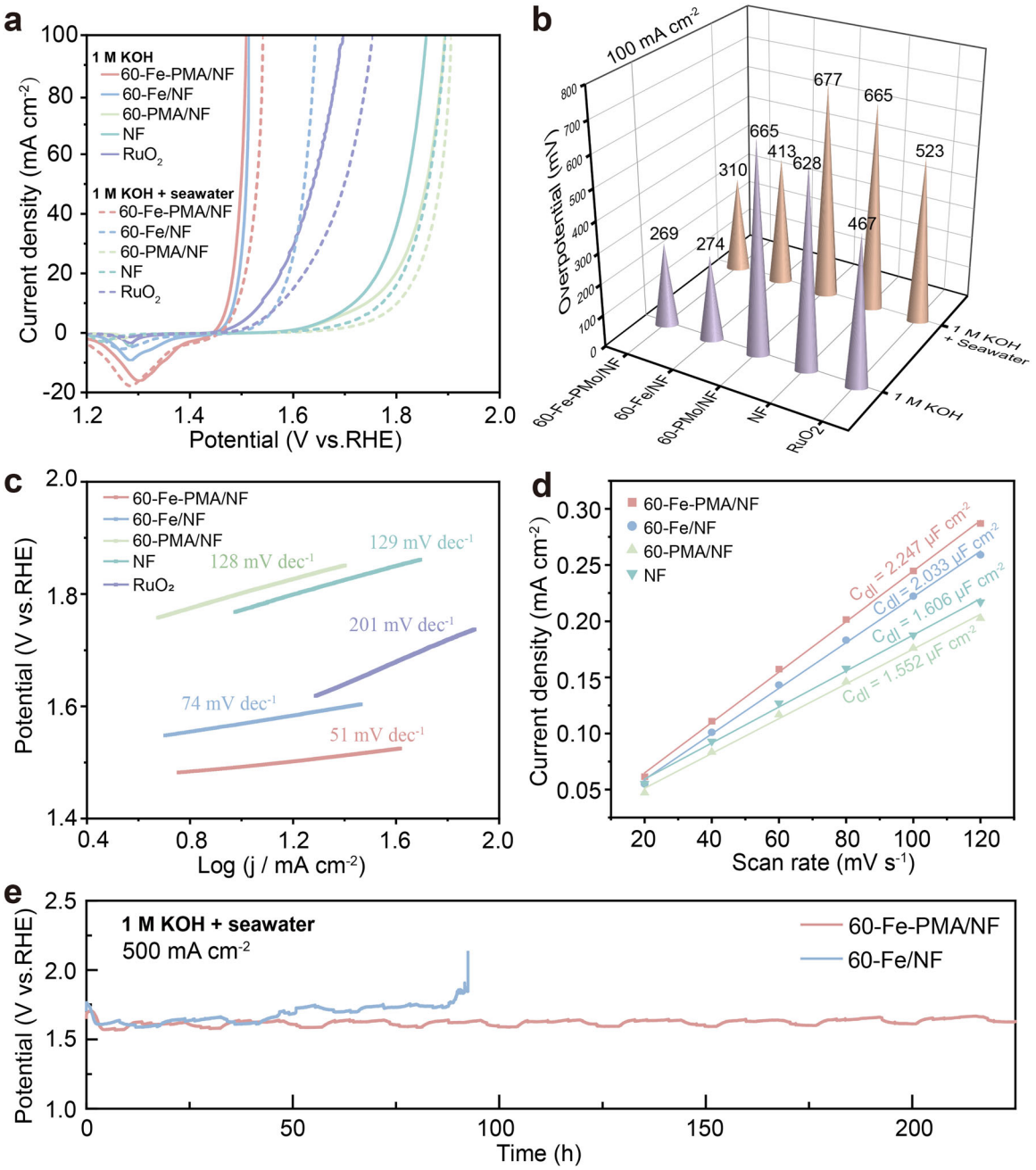

FIGURE 2 | Superior OER performance and stability of 60-Fe-PMA/NF in alkaline seawater. (a) *iR*-corrected LSV polarization curves (5 mV s^{-1}) in 1 M KOH and alkaline seawater (1 M KOH + seawater) for 60-Fe-PMA/NF versus controls (NF, 60-Fe/NF, 60-PMA/NF, RuO_2). (b) Overpotentials at 100 mA cm^{-2} highlighting 60-Fe-PMA/NF's exceptional activity. (c) Tafel slopes quantifying accelerated kinetics (51 mV dec^{-1} for 60-Fe-PMA/NF). (d) Electrochemical double-layer capacitance (C_{dl}) measurements from cyclic voltammetry at non-Faradaic potentials. (e) Chronopotentiometric stability test of 60-Fe/NF and 60-Fe-PMA/NF at 500 mA cm^{-2} in 1.0 M KOH + seawater.

100 mA cm^{-2} in alkaline seawater, substantially higher than 60-Fe-PMA/NF (Figure S9), highlighting the catalyst's exceptional activity under realistic operating conditions.

Systematic optimization identified 0.002 M PMA with 60-s immersion as the optimal condition, determined through LSV analysis of PMA concentrations (0.001–0.01 M) and immersion times (10–300 s) with fixed 0.1 M $FeCl_3$ (Figures S10 and S11). This optimized 60-Fe-PMA/NF configuration delivers lower overpotentials than most recently reported Ni foam-based seawater OER catalysts (Table S2), establishing state-of-the-art performance for direct seawater electrolysis.

Further kinetic analysis demonstrates enhanced reaction mechanisms. The Tafel slope decreases to 51 mV dec^{-1} for 60-Fe-PMA/NF (Figure 2c), substantially lower than bare NF (129 mV dec^{-1}), indicating accelerated charge transfer kinetics. Electrochemical double-layer capacitance (C_{dl}) measurements confirm PMA incorporation simultaneously expands the electrochemically active surface area and boosts intrinsic activity through

Fe–PMA synergy (Figures 2d and S12). These results collectively demonstrate that PMA introduction optimizes active site density, enhances charge transfer, and confers essential chloride resistance — addressing three critical challenges in seawater splitting systems.

Chronopotentiometric measurements at industrially relevant 500 mA cm^{-2} in alkaline seawater (Figure 2e) reveal 60-Fe-PMA/NF operates stably for >200 hours with negligible voltage drift, while the PMA-free 60-Fe/NF control degrades within 90 h. This stark contrast underscores PMA's indispensable role in stabilizing catalytic interfaces under seawater conditions.

Control experiments replacing PMA with phosphoric acid/molybdic acid mixtures, phosphotungstic acid (PTA), or silicomolybdic acid (SMA) confirm that only PMA-containing catalysts achieve optimal activity (Figure S13). Specifically, PMA-modified electrodes require 312 mV lower overpotential at 100 mA cm^{-2} compared to phosphoric acid/molybdic acid mixtures, highlighting the critical advantage of PMA's intact polyanionic structure over its constituent components.

2.3 | Mechanistic Insights into Seawater OER Performance of 60-Fe-PMA/NF

Optimal OER requires balanced electrode wettability and aerophobicity to maximize active site exposure, intermediate adsorption, and mass transfer [19]. Dynamic contact angle measurements (Figure 3a) reveal that 60-Fe-PMA/NF exhibits superhydrophilicity (water contact angle: 0° vs 131.8° for pristine NF) and enhanced aerophobicity (air contact angle: 151.7° vs 140.9°), collectively promoting water adsorption while accelerating oxygen bubble detachment to boost catalytic activity.

Operando electrochemical impedance spectroscopy (EIS) performed during OER (Figures 3b–c; Figure S14) demonstrates that 60-Fe-PMA/NF achieves significantly lower charge transfer resistance (R_{CT}) than 60-Fe/NF at equivalent potentials [20]. This accelerated charge transfer is corroborated by Bode plot analysis (Figures 3b–c), where the phase angle decreases more rapidly with increasing potential, indicating faster hydroxide-to-oxyhydroxide transition [21, 22] and improved reaction kinetics [23].

In situ Raman spectroscopy in alkaline seawater (Figures 3d–e) confirms γ-NiOOH formation (characteristic peaks at 475/557 cm^{-1}) as the catalytically active phase. Crucially, 60-Fe-PMA/NF exhibits enhanced γ-NiOOH generation compared to 60-Fe/NF at identical potentials, demonstrating PMA's role in promoting surface reconstruction. This γ-NiOOH phase enhances OER activity through its larger interlayer spacing and higher Ni(III) oxidation state, which collectively facilitate an amorphous structure with unsaturated coordination sites to accelerate nucleophilic adsorption of hydroxyl intermediates [24]. Simultaneously, the interlayer structure accommodates dissociable species (H_2O, OH^-), promoting reactant binding to active Ni(III) sites [25, 26]. Compared with the 60-Fe/NF, 60-Fe-PMA/NF exhibits a clear blue shift of the Ni–O stretching vibrations under 1.6 V, with the E_g mode shifting from 474 to 476 cm^{-1} and the A_{1g} mode from 556 to 558 cm^{-1}. This shift indicates an increased Ni–O bond force constant. Stronger Ni–O bonds enhance OER intermediate kinetics and structural stability in chloride-containing electrolytes [27].

Inductively coupled plasma optical emission spectroscopy (ICP-OES) and XPS analyses collectively reveal dynamic phosphorus leaching-reabsorption behavior in 60-Fe-PMA/NF. Before OER initiation, alkaline seawater immersion induces moderate phosphorus leaching (0.27 mg L^{-1}) with minimal molybdenum release (0.06 mg L^{-1}) into the electrolyte (Figure 3f). Corresponding XPS analysis confirms abundant PO_4^{3-} and Mo^{6+} species remain on the catalyst surface post-immersion (Figure 3g). Upon OER commencement, rapid elemental leaching occurs within 0.5 h, with phosphorus levels surging to 1.33 mg $L^{-1}$and molybdenum to 7.14 mg L^{-1} in the electrolyte.

Notably, molybdenum concentration in electrolyte peaks at ≈ 7.8 mg L^{-1} by 2 h and stabilizes thereafter. In contrast, phosphorus concentration peaks at 1.33 mg L^{-1} (0.5 h), then progressively decreases to 0.98 mg L^{-1} (2 h) and 0.82 mg L^{-1} (12 h), signifying the reabsorption of PO_4^{3-} species—generated through PMA degradation [17]—into the catalyst matrix. Post-operation XPS analysis confirms this differential behavior (Figure 3g): a significant amount of phosphorus is retained on the catalyst surface after 12 h of OER, while molybdenum content markedly decreases. In situ Raman spectroscopy, performed on the 60-Fe-PMA/NF electrode in alkaline simulated seawater (1 M KOH + 0.5 M NaCl) to minimize spectral interference from complex oxyanions, provides direct insight into the dynamic interfacial process (Figure S15). Under constant anodic polarization, phosphate-related vibrational features gradually intensify and eventually stabilize, consistent with the re-adsorption of phosphorus-containing species observed in the electrolyte and on the catalyst surface. This selective phosphorus reabsorption likely contributes to the exceptional stability of 60-Fe-PMA/NF, as PO_4^{3-} species are established stabilizers of nickel-based catalysts in seawater environments [28, 29].

Tafel analysis in alkaline seawater (Figure 3h) further demonstrates that 60-Fe-PMA/NF achieves a more positive corrosion potential and lower corrosion current density than 60-Fe/NF. This corrosion resistance originates from PMA-promoted γ-NiOOH formation, where the strong Lewis acidity of γ-NiOOH preferentially adsorbs OH^- over Cl^- via the hard-soft acid-base (HSAB) principle, thereby inhibiting chloride corrosion [30, 31]. Simultaneously, phosphate-rich interfaces from reabsorbed P species block Cl^- adsorption [28]. Thus, PMA synergistically enhances activity through surface reconstruction while conferring stability via dynamic self-healing and chloride exclusion mechanisms.

2.4 | Zero-Gap Alkaline Seawater Electrolyzer Performance

To validate industrial applicability, we constructed a zero-gap electrolyzer with asymmetric alkaline seawater configuration using 60-Fe-PMA/NF as the anode and commercial nickel-molybdenum foam (NiMo) as the cathode (Figure 4a). A control system with Raney Ni(+)||NiMo(-) electrodes was assembled

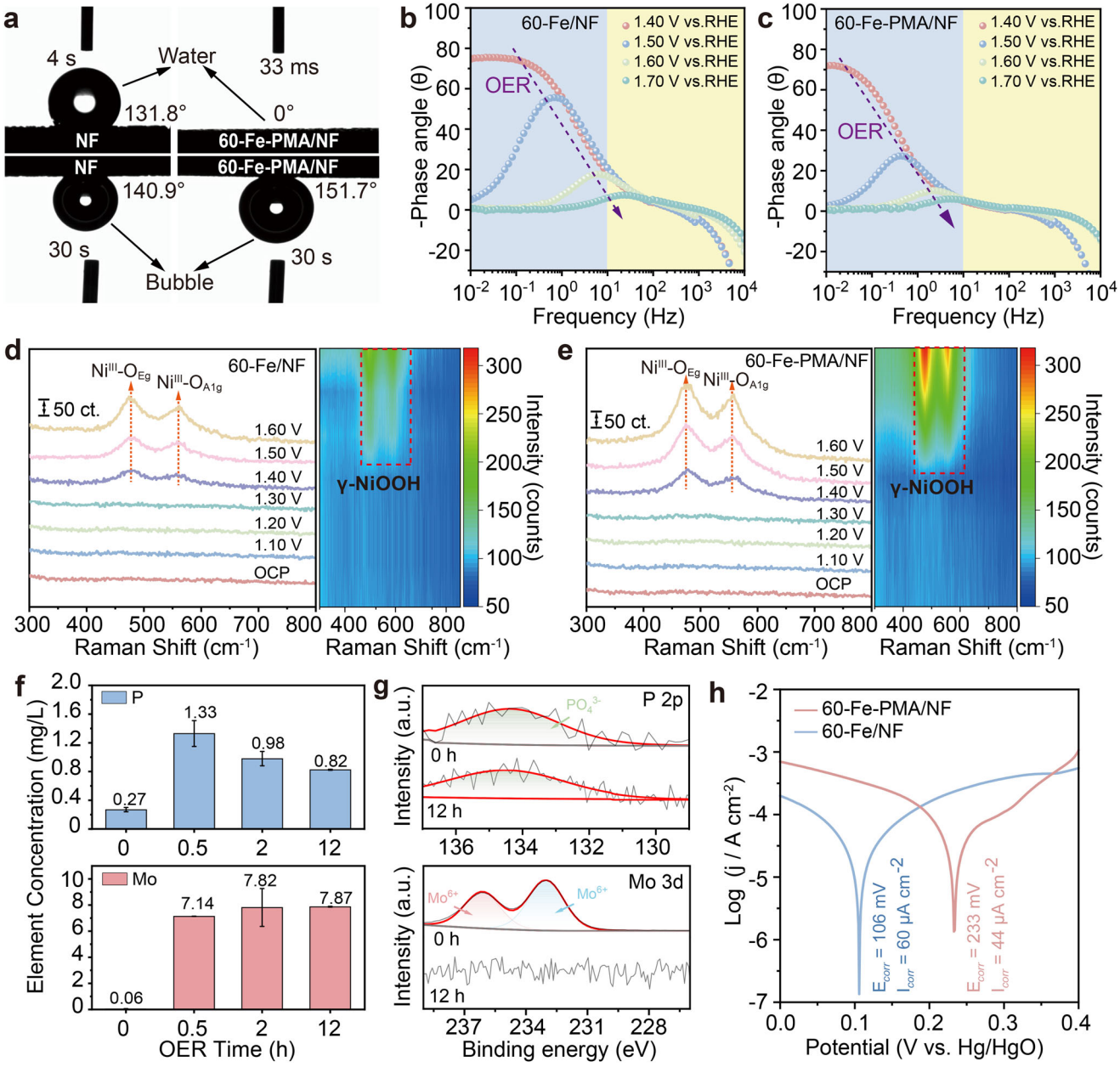

FIGURE 3 | Mechanistic origins of enhanced activity and stability. (a) Solid–liquid/gas contact angles demonstrating superhydrophilicity (0°) and aerophobicity (151.7°) of 60-Fe-PMA/NF versus bare NF. (b,c) Operando EIS Bode phase plots under OER conditions in alkaline seawater, showing accelerated charge transfer kinetics for 60-Fe-PMA/NF (c) over 60-Fe/NF (b). (d,e) In situ Raman spectra confirming PMA-promoted γ-NiOOH formation (475/557 cm^{-1}) during seawater OER. (f) ICP-OES quantification of the Mo/P concentrations in the electrolyte, showing the dynamic phosphorus leaching-reabsorption behavior. Data points represent the mean values from n = 3 independent measurements. (g) XPS analysis revealing phosphorus and molybdate evolution on catalyst surfaces. (h) Tafel plots demonstrating superior chloride corrosion resistance in alkaline seawater.

for comparison. Remarkably, the 60-Fe-PMA/NF(+)||NiMo(-) configuration achieved significantly lower cell voltages of 2.35 V (at 0.5 A cm^{-2}), 2.83 V (at 1.0 A cm^{-2}), and 3.21 V (at 1.5 A cm^{-2})—outperforming the Raney Ni-based system under identical conditions (Figure 4b). This voltage reduction highlights the exceptional catalytic activity of 60-Fe-PMA/NF in industrially relevant, zero-gap seawater electrolyzers.

Long-term stability tests at 1.0 A cm^{-2} revealed 60-Fe-PMA/NF(+)||NiMo(-) maintains stable operation for over 270 h with negligible voltage drift (Figure 4c), demonstrating exceptional durability for seawater electrolysis. Faradaic efficiency measurements confirmed robust performance, maintaining values above 98% throughout the testing period. In stark contrast, the Raney Ni(+)||NiMo(-) system exhibited rapid voltage degradation within minutes, culminating in complete failure. Analysis of the electrolyte after the stability test shows that residual hypochlorite (ClO^-), quantified via the DPD spectrophotometric method at 515 and 555 nm, is markedly lower for 60-Fe-PMA/NF than for Raney Ni (Figure S16). This indicates substantially less ClO^- formation and effective suppression of chloride oxidation, highlighting the catalyst's exceptional

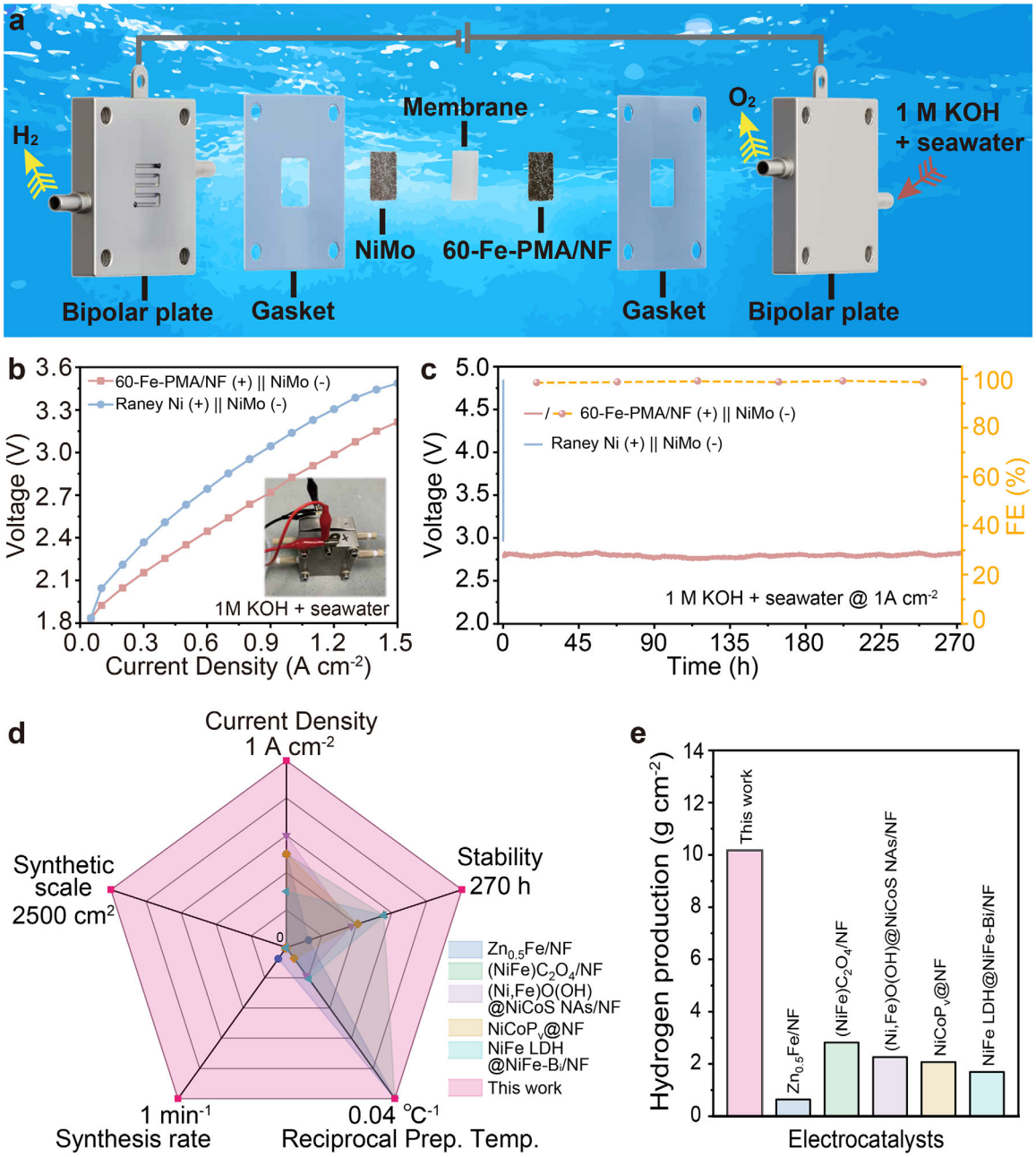

FIGURE 4 | Zero-gap alkaline electrolyzer configuration and performance. (a) Schematic of asymmetric alkaline seawater configuration. (b) Linear sweep voltammetry curves of the membrane electrode assembly (MEA) flow electrolyzer, showing superior voltage efficiency (2.83 V at 1.0 A cm^{-2}) for 60-Fe-PMA/NF(+)||NiMo(-) vs. Raney Ni(+)||NiMo(-). (c) Chronopotentiometric stability at 1.0 A cm^{-2} demonstrating >270 h continuous operation for 60-Fe-PMA/NF(+)||NiMo(-) versus rapid failure of Raney Ni control. (d) Comprehensive benchmarking against state-of-the-art seawater OER catalysts: current density, stability duration, synthesis temperature/rate, and electrode dimensions. (e) Lifetime hydrogen production capacity comparison with reported systems.

operational stability under harsh seawater electrolysis conditions.

This zero-gap seawater electrolyzer demonstrates remarkable durability surpassing most existing alkaline seawater systems (Figure 4d) [25, 32–35] while the ultrafast, scalable catalyst synthesis enables practical industrial deployment. Quantitative analysis revealed a total hydrogen production capacity of 10.15 g cm^{-2}, significantly exceeding conventional electrolyzers (Figure 4e). Collectively, these results establish 60-Fe-PMA/NF as a transformative platform for industrial-scale hydrogen production—uniting superior seawater OER activity, extraordinary durability, and ultrafast, scalable fabrication.

3 | Conclusions

We developed a novel methodology leveraging phosphomolybdic acid (PMA) cluster chemistry for ultrafast surface reconstruction of nickel-based electrodes, enabling high-performance oxygen

evolution catalysts. This rapid, solution-based synthesis strategy offers four critical advantages: ambient-temperature conditions, 60-s processing, meter-scale manufacturability, and elimination of specialized equipment.

Comprehensive mechanistic studies reveal that synergistic trace Fe incorporation, PMA-induced superhydrophilicity, and dynamic PMA leaching–reabsorption in alkaline electrolytes drive extensive surface reconstruction. This process simultaneously enhances active-site density, while suppressing chloride-induced corrosion and impurity adsorption—collectively boosting OER activity and durability in seawater electrolysis.

The optimized 60-Fe-PMA/NF catalyst exhibits industrial-grade durability when integrated into a precious-metal-free zero-gap alkaline seawater electrolyzer (60-Fe-PMA/NF(+)||NiMo(-)) configuration. This system demonstrates exceptional stability, exceeding 270 h of continuous operation at ampere-level current density (1.0 A cm^{-2}).

Combining ultralow material cost with facile, scalable fabrication, this approach establishes a transformative paradigm for industrial seawater electrolysis. Our work bridges fundamental catalyst design and practical implementation, providing a scalable, cost-effective pathway to sustainable hydrogen production directly from seawater.

4 | Experimental Section

Experimental details can be found in the Supporting information.

Author Contributions

Credit: X. Huang, conceptualization, data curation, methodology, formal analysis, investigation, visualization, writing – original draft; L. Chen, investigation; Y. Li, resources; Y. Liu, characterization; H. Zhang, validation; L. Li, validation; Y. Wang, conceptualization, funding acquisition, supervision, validation, visualization, writing – review & editing.

Acknowledgments

Y.W. acknowledged the funding support from National Key R&D Program of China (2023YFA1509001), National Natural Science Foundation of China (22250004), Guangdong Innovative and Entrepreneurial Research Team Program (2023ZT10C139), Guangzhou Basic and Applied Basic Research Foundation (2024D03J0007), and PCOSS Open Project (202202).

Conflicts of Interest

The authors declare no conflicts of interest.

Data Availability Statement

The data that support the findings of this study are available in the supplementary material of this article.

References

1. T. Terlouw, L. Rosa, C. Bauer, and R. McKenna, "Future Hydrogen Economies Imply Environmental Trade-Offs and a Supply–Demand Mismatch," *Nature Communications* 15 (2024): 7043.

2. G. Glenk and S. Reichelstein, "Economics of Converting Renewable Power to Hydrogen," *Nature Energy* 4 (2019): 216–222.

3. G. Bahuguna and F. Patolsky, "Enabling Unprecedented Ultra-Efficient Practical Direct Seawater Splitting by Finely Tuned Catalyst Environment via Thermo-Hydrodynamic Modulation," *Advanced Energy Materials* 13 (2023): 2301907.

4. X. Gao, J. Chen, Y. Yu, et al., "Core–Shell Structured NiTe@FeOOH Nanoarrays for Efficient Overall Seawater Splitting," *Chemical Engineering Journal* 474 (2023): 145568.

5. Y. Yao, C. Yang, S. Sun, et al., "Boosting Alkaline Seawater Oxidation of CoFe-Layered Double Hydroxide Nanosheet Array by Cr Doping," *Small* 20 (2024): 2307294.

6. H. Zhou, F. Yu, Q. Zhu, et al., "Water Splitting by Electrolysis at High Current Densities under 1.6 Volts," *Energy & Environmental Science* 11 (2018): 2858–2864.

7. X. Kang, F. Yang, Z. Zhang, et al., "A Corrosion-Resistant RuMoNi Catalyst for Efficient and Long-Lasting Seawater Oxidation and Anion Exchange Membrane Electrolyzer," *Nature Communications* 14 (2023): 3607.

8. S. Ding, Z. Li, G. Lin, L. Wang, A. Dong, and L. Sun, "Enhancing Mass Transfer in Anion Exchange Membrane Water Electrolysis by Overlaid Nickel Mesh Substrate," *ACS Energy Letters* 9 (2024): 3719–3726.

9. W. J. F. Gannon and C. W. Dunnill, "Raney Nickel 2.0: Development of a High-Performance Bifunctional Electrocatalyst," *Electrochimica Acta* 322 (2019): 134687.

10. Y. Bao, Z. Wu, B. Liu, et al., "Fe-Doped Ni3S2 Nanosheets on Ni Foam for Alkaline Seawater Oxidation," *ACS Applied Nano Materials* 6 (2023): 4360–4369.

11. W. Liu, J. Bao, M. Guan, et al., "Nickel–Cobalt-Layered Double Hydroxide Nanosheet Arrays on Ni Foam as a Bifunctional Electrocatalyst for Overall Water Splitting," *Dalton Transactions* 46 (2017): 8372–8376.

12. L. Liu, Y. Chen, Q. Zhang, et al., "Superhydrophilic NiFe-LDH@Co9S8-Ni3S2/NF Heterostructures for High-Current-Density Freshwater/Seawater Oxidation Electrocatalysts," *Applied Catalysis B* 354 (2024): 124140.

13. M. Qi, M. Qin, H. Wang, et al., "Regulating the Redox Cycle of Nickel Species for Efficient Seawater Electrolysis," *Applied Catalysis B* 356 (2024): 124259.

14. L. Yu, L. Wu, B. McElhenny, et al., "Ultrafast Room-Temperature Synthesis of Porous S-Doped Ni/Fe (Oxy)hydroxide Electrodes for Oxygen Evolution Catalysis in Seawater Splitting," *Energy & Environmental Science* 13 (2020): 3439–3446.

15. Y. Zhuo, D. Liu, L. Qiao, et al., "Ultrafast Room-Temperature Synthesis of Large-Scale, Low-Cost, and Highly Active Ni–Fe-Based Electrodes toward Industrialized Seawater Oxidation," *Advanced Energy Materials* 13 (2023): 2301921.

16. F. Lyu, S. Zeng, Z. Jia, et al., "Two-Dimensional Mineral Hydrogel-Derived Single-Atoms-Anchored Heterostructures for Ultrastable Hydrogen Evolution," *Nature Communications* 13 (2022): 6249.

17. Z. Cai, P. Wang, J. Zhang, et al., "Reinforced Layered Double Hydroxide Oxygen-Evolution Electrocatalysts: A Polyoxometallic Acid Wet-Etching Approach and Synergistic Mechanism," *Advanced Materials* 34 (2022): 2110696.

18. X. Cao, Y. Ding, D. Chen, W. Ye, W. Yang, and L. Sun, "Cluster-Level Heterostructure of PMo12/Cu for Efficient and Selective Electrocatalytic Hydrogenation of High-Concentration 5-Hydroxymethylfurfural," *Journal of the American Chemical Society* 146 (2024): 25 125–25 136.

19. C. Zhang, Z. Guo, Y. Tian, C. Yu, K. Liu, and L. Jiang, "Engineering Electrode Wettability to Enhance Mass Transfer in Hydrogen Evolution Reaction," *Nano Research Energy* 2 (2023): e9120063.

20. N. Zhang, Y. Hu, L. An, et al., "Surface Activation and Ni–S Stabilization in NiO/NiS2 for Efficient Oxygen Evolution Reaction," *Angewandte Chemie International Edition* 61 (2022): e202207217.

21. L. Guo, Z. Zhang, Z. Mu, et al., "Ceria-Optimized Oxygen-Species Exchange in Hierarchical Bimetallic Hydroxide for Electrocatalytic Water Oxidation," *Advanced Materials* 36 (2024): 2406682.

22. J. Wang, Y. Liu, G. Yang, et al., "MXene-Assisted NiFe Sulfides for High-Performance Anion Exchange Membrane Seawater Electrolysis," *Nature Communications* 16 (2025): 1319.

23. Z. Xiao, Y.-C. Huang, C.-L. Dong, et al., "Operando Identification of the Dynamic Behavior of Oxygen Vacancy-Rich Co3O4 for Oxygen Evolution Reaction," *Journal of the American Chemical Society* 142 (2020): 12 087–12 095.

24. R. L. Doyle, I. J. Godwin, M. P. Brandon, and M. E. G. Lyons, "Redox and Electrochemical Water Splitting Catalytic Properties of Hydrated Metal Oxide Modified Electrodes," *Physical Chemistry Chemical Physics* 15 (2013): 13 737–13 783.

25. J. Na, H. Yu, S. Jia, et al., "Electrochemical Reconstruction of Non-Noble Metal-Based Heterostructure Nanorod Array Electrodes for Highly Stable Anion Exchange Membrane Seawater Electrolysis," *Journal of Energy Chemistry* 91 (2024): 370–382.

26. J. Li, Y. Liu, H. Chen, Z. Zhang, and X. Zou, "Design of a Multilayered Oxygen-Evolution Electrode with High Catalytic Activity and Corrosion Resistance for Saline Water Splitting," *Advanced Functional Materials* 31 (2021): 2101820.

27. Q. Niu, F.-Y. Gao, X. Sun, Y. Zheng, and S.-Z. Qiao, "Chloride-Mediated Electron Buffering on Ni–Fe Anodes for Ampere-Level Alkaline Seawater Electrolysis," *Advanced Functional Materials* 35 (2025): 2504872.

28. R. Fan, C. Liu, Z. Li, et al., "Ultrastable Electrocatalytic Seawater Splitting at Ampere-Level Current Density," *Nature Sustainability* 7 (2024): 158–167.

29. H. Komiya, K. Obata, T. Honma, and K. Takanabe, "Dynamic Stabilization of Nickel-Based Oxygen Evolution Electrocatalysts in the Presence of Chloride Ions Using a Phosphate Additive," *Journal of Materials Chemistry A* 12 (2024): 3513–3522.

30. Z. Qiu, Y. Ma, and T. Edvinsson, "In Operando Raman Investigation of Fe Doping Influence on Catalytic NiO Intermediates for Enhanced Overall Water Splitting," *Nano Energy* 66 (2019): 104118.

31. J. Guo, Y. Zheng, Z. Hu, et al., "Direct Seawater Electrolysis by Adjusting the Local Reaction Environment of a Catalyst," *Nature Energy* 8 (2023): 264–272.

32. N. Yu, J. Y. Lv, Z.-C. Guo, et al., "Strong Lewis Acid-Induced Self-Healing of Loose FeOOH for Alkaline Oxygen Evolution," *Chemical Engineering Journal* 487 (2024): 150253.

33. Z. Li, Y. Yao, S. Sun, et al., "Carbon Oxyanion Self-Transformation on NiFe Oxalates Enables Long-Term Ampere-Level Current Density Seawater Oxidation," *Angewandte Chemie International Edition* 63 (2024): e202316522.

34. T. Li, C. Yang, Z. Cai, et al., "Surface Borate Layer Dramatically Enhances the Stability of NiFe-Layered Double Hydroxide for Alkaline Seawater Oxidation," *Materials Today Physics* 50 (2025): 101612.

35. L. Guo, J. Chi, T. Cui, et al., "Phosphorus-Defect-Mediated Electron Redistribution to Boost Anion Exchange Membrane-Based Alkaline Seawater Electrolysis," *Advanced Energy Materials* 14 (2024): 2400975.

Supporting Information

Additional supporting information can be found online in the Supporting Information section.

Supporting Information smll72323-sup-0001-SuppMat.docx.